Supplemental Material for: Femtosecond X-ray scattering study of ultrafast photoinduced structural dynamics in solvated $[Co(terpy)_2]^{2+}$

Elisa Biasin,[1] Tim Brandt van Driel,[1] Kasper S. Kjær,[1,2,3] Asmus O. Dohn,[4] Morten Christensen,[1] Tobias Harlang,[2] Pavel Chabera,[2] Yizhu Liu,[2,5] Jens Uhlig,[2] Mátyás Pápai,[4,6] Zoltán Németh,[6] Robert Hartsock,[3] Winnie Liang,[3] Jianxin Zhang,[7] Roberto Alonso-Mori,[8] Matthieu Chollet,[8] James M. Glownia,[8] Silke Nelson,[8] Dimosthenis Sokaras,[8] Tadesse A. Assefa,[9] Alexander Britz,[9] Andreas Galler,[9] Wojciech Gawelda,[9,10] Christian Bressler,[9] Kelly J. Gaffney,[3] Henrik T. Lemke,[8,11] Klaus B. Møller,[4] Martin M. Nielsen,[1] Villy Sundström,[2] György Vankó,[6] Kenneth Wärnmark,[5] Sophie E. Canton,[12,13] and Kristoffer Haldrup[1]

[1] *Technical University of Denmark, Department of Physics, Fysikvej 307, DK-2800 Kongens Lyngby, Denmark.*

[2] *Department of Chemical Physics, Lund University, Box 118, S-22100 Lund, Sweden.*

[3] *PULSE Institute, SLAC National Accelerator Laboratory, Menlo Park, CA 94025, USA.*

[4] *Technical University of Denmark, Department of Chemistry, Kemitorvet 207, DK-2800 Kongens Lyngby, Denmark.*

[5] *Centre for Analysis and Synthesis, Department of Chemistry, Lund University, Box 124, Lund SE-22100, Sweden.*

[6] *Wigner Research Centre for Physics, Hungarian Academy Sciences, H-1525 Budapest, Hungary.*

[7] *School of Environmental and Chemical Engineering, Tianjin Polytechnic University, Tianjin 300387, China*

[8] *LCLS, SLAC National Accelerator Laboratory, Menlo Park, CA 94025, USA.*

[9] *European XFEL GmbH, Albert-Einstein-Ring 19, D-22761 Hamburg, Germany.*

[10] *Institute of Physics, Jan Kochanowski University, 25-406 Kielce, Poland.*

[11] *SwissFEL, Paul Scherrer Institut, 5232 Villigen PSI, Switzerland.*

[12] *IFG Structural Dynamics of (Bio)chemical Systems, Max Planck Institute for Biophysical Chemistry, Am Fassberg 11, D-37077 Goettingen, Germany*

[13] *FS-SCS, Structural Dynamics with Ultra-short Pulsed X-rays,*
Deutsches Elektronen-Synchrotron (DESY),
Notkestrasse 85, D-22607 Hamburg, Germany

CONTENTS

I. MODEL AND FIT OF THE DATA

As described in the article, the measured difference scattering signal is modelled as

$$\Delta S_{model}(Q,\, t) = \alpha(t)\Delta S_{str.}(Q,\, t) + \Delta S_{solvent}(Q,t) \tag{S1}$$

where $\Delta S_{str.}(Q,\, t) = \Delta S_{solute}(Q,\, t) + \Delta S_{cage}(Q)$, arising from the structural response of the system, and $\Delta S_{solvent}(Q,t) = \Delta T(t)\frac{\partial S(Q)}{\partial T}\Big|_{\rho} + \Delta\rho(t)\frac{\partial S(Q)}{\partial \rho}\Big|_{T}$, describing the changes in X-ray scattering arising from the temperature increase and the density changes of the bulk solvent. In this expression, α represents the excitation fraction and ΔT and $\Delta\rho$ the increase in solvent temperature and density, respectively.

A. Bulk solvent contributions

Fig.S1(a) shows the solvent contributions to the difference scattering signal: $\left.\frac{\partial S(Q)}{\partial T}\right|_{\rho}$ and $\left.\frac{\partial S(Q)}{\partial \rho}\right|_{T}$ from [1, 2]. Fig. S1(b) shows ΔT and $\Delta\rho$ obtained as a function of time when using the expression in Eq. S1 to fit the experimental data presented in the article (Fig.2 (a)). We note that the solvent contribution to the recorded difference scattering signal is completely dominated by the change in scattering arising from the temperature increase, while the contribution from density changes is found to be negligible (less then 0.025 kg·m^{-3}). Therefore, only the former was used in the analysis (Eq.6).

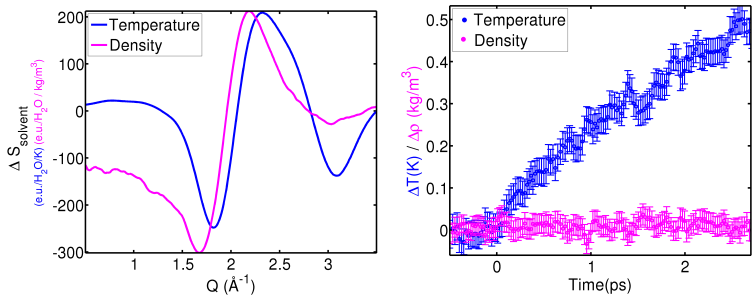

Figure S1. **a:** Measured solvent differentials for water describing the change in difference scattering signal arising from change in temperature (blue) and density (magenta), from [2]. **b:** Fit results for ΔT and $\Delta\rho$ obtained when fitting Eq. S1 to the experimental data in Fig.2(a).

B. Structure and excitation fraction

The scattering signal from the solute molecule (Eq.3) is calculated through the Debye equation:

$$S(Q) = \sum_{i}^{N} |f_i(Q)|^2 + 2\sum_{i<j}^{N} f_i(Q) f_j(Q) \frac{\sin(Q r_{ij})}{Q r_{ij}} \tag{S2}$$

where N is the number of atoms in the molecule, $f_i(Q)$ the atomic form factor for atom i and r_{ij} describe the inter-atomic distances [3].

As discussed in our previous work [4], a strong correlation is often found between the excitation fraction and the magnitude of the structural changes when expressions such as Eq. S1 are used to fit the acquired difference signals. In the present analysis, the simultaneous

determination of both the excitation fraction α and the structural parameter $d_{\text{Co-N}}$ in Eq.6 is significantly improved by assuming the temporal profile of α (Eq.7) and simultaneously optimizing the excited-state molecular structure in a 'global' framework that includes all time delays in the structural analysis [5].

With respect to Eq.7 in the main text, the full expression used to describe the temporal evolution of the the excitation fraction is:

$$\alpha(\mathrm{t}) = \int_{-\infty}^{+\infty} \frac{1}{\sigma_{\text{IRF}}\sqrt{2\pi}} e^{\frac{-(\mathrm{t}-y)^2}{2\sigma_{\text{IRF}}^2}} H(y-\mathrm{t}_0) A e^{-\frac{y-\mathrm{t}_0}{\tau}} dy \tag{S3}$$

where σ_{IRF} is the width of the Gaussian IRF, A and τ are the amplitude and the lifetime of the exponential function, describing respectively the initial amplitude (excitation fraction) and subsequent decay of the bond-elongated excited state, t_0 is the starting point of the exponential decay and y is the integration variable.

Fig.3 of the main article shows the changes in the axial Co-N distance after photoexcitation. The time evolution of this parameter is well described by two oscillations superimposed on an exponential decay, all convoluted with the Gaussian IRF of width σ_{IRF}:

$$\begin{aligned}
\Delta d_{\text{Co-Naxial}}(\mathrm{t}) &= \mathrm{IRF}(\sigma_{\text{IRF}}, \mathrm{t}) \otimes [E e^{-\frac{\mathrm{t}-\mathrm{t}_0}{\tau_R}} + B_1 e^{-\frac{\mathrm{t}-\mathrm{t}_0}{\tau_O}} \cos(\frac{2\pi(\mathrm{t}-\mathrm{t}_0)}{T_1} + f_1) + \\
&\quad + (1 - e^{-\frac{\mathrm{t}-\mathrm{t}_0}{\tau_O}}) B_2 \cos(\frac{2\pi(\mathrm{t}-\mathrm{t}_0)}{T_2} + f_2)] \cdot H(\mathrm{t}-\mathrm{t}_0) \\
&= \int_{\mathrm{t}_0}^{+\infty} \frac{1}{\sigma_{\text{IRF}}\sqrt{2\pi}} e^{-\frac{(\mathrm{t}-y)^2}{2\sigma_{\text{IRF}}^2}} [E e^{-\frac{y-\mathrm{t}_0}{\tau_R}} + B_1 e^{-\frac{y-\mathrm{t}_0}{\tau_O}} \cos(\frac{2\pi(y-\mathrm{t}_0)}{T_1} + f_1) + \\
&\quad + (1 - e^{-\frac{y-\mathrm{t}_0}{\tau_O}}) B_2 \cos(\frac{2\pi(y-\mathrm{t}_0)}{T_2} + f_2)] dy
\end{aligned} \tag{S4}$$

where E and τ_R are the amplitude and the lifetime of the exponential decay, B_1, T_1 and f_1 are, respectively, the amplitude, the period and the phase of the first oscillation, and B_2, T_2 and f_2 are, respectively, the amplitude, the period and the phase of the second oscillation. τ_O is the dampening time of the first oscillation as well as the grow-in time of the second one, and y is the integration variable. The best-fit parameters obtained by fitting this expression to $\Delta d_{\text{Co-Naxial}}$ are reported in Table S1. The (adjusted) R^2 is found 0.88. We note that E describes the difference between $d_{\text{Co-Naxial}}$ of the bond-elongated excited state at time zero and the average value of the same quantity after 2 ps. This latter value for $d_{\text{Co-Naxial}}$ is interpreted as the axial Co-N bond length of the HS structure and used in the fit of the long time range dataset (Section V).

σ_{IRF} (ps)	0.05 (fixed)
t_0 (ps)	-0.01 (fixed)
E (Å)	0.014 ± 0.002
τ_R (ps)	0.7 ± 0.1
B (Å)	0.03 ± 0.01
τ_O (ps)	0.4 ± 0.1
T (ps)	0.33 ± 0.03
f (a.u)	- 4.4 ± 0.4
B_2 (Å)	0.002 ± 0.003
T_2 (ps)	0.23 ± 0.01
f_2 (a.u)	0.7 ± 0.7

Table S1. Fit results (95 % confidence bounds) after fitting the expression in Eq. S4 to $\Delta \mathrm{d}_{\text{Co-Naxial}}(\mathrm{t})$ (Fig.3).

C. Bulk solvent kinetics

Fig. S2 shows the temporal evolution of $\Delta\mathrm{T}(\mathrm{t})$ (black points). The data are described through the expression:

$$\Delta \mathrm{T}(\mathrm{t}) = \mathrm{IRF}(\sigma_{\mathrm{IRF}}, \mathrm{t}) \otimes H(\mathrm{t}-\mathrm{t}_0) \sum_{j=1}^{N} \gamma_j (1 - e^{-\frac{\mathrm{t}-\mathrm{t}_0}{\tau_j}}) \tag{S5}$$

$$= \int_{\mathrm{t}_0}^{+\infty} \frac{1}{\sigma_{\mathrm{IRF}}\sqrt{2\pi}} e^{-\frac{(\mathrm{t}-y)^2}{2\sigma_{\mathrm{IRF}}^2}} \sum_{j=1}^{N} \gamma_j (1 - e^{-\frac{y-\mathrm{t}_0}{\tau_j}}) dy$$

where σ_{IRF} is the width of the Gaussian IRF, γ and τ are the amplitude and the lifetime of the N exponential functions and H is the Heaviside step function centered at t_0. Fig. S2 shows a comparison between using a single (N=1) or a double (N=2) exponential function to describe the short time range dataset and we find that the latter better describes the time evolution of ΔT in the first hundreds of femtoseconds. A single exponential grow-in is used to fit the long time range measurements (see Fig. S8). The parameters obtained for both datasets are reported in Tab. S2.

	short time range	long time range
σ_{IRF} (ps)	0.05 (fixed)	0.05 (fixed)
t_0 (ps)	-0.01 (fixed)	-0.01 (fixed)
γ_1 (K)	0.05 $\pm$ 0.2	/
τ_1 (ps)	0.01 $\pm$ 0.9	/
γ_2 (K)	0.8 $\pm$ 0.3	0.84 $\pm$ 0.02
τ_2 (ps)	3.5 $\pm$ 0.8	4.0 $\pm$ 0.6

Table S2. Fit results (95 % confidence bounds) after fitting the expression in Eq. S5 to ΔT(t) both in the short (Fig.S2) and the long (Fig. S8(b)) time range.

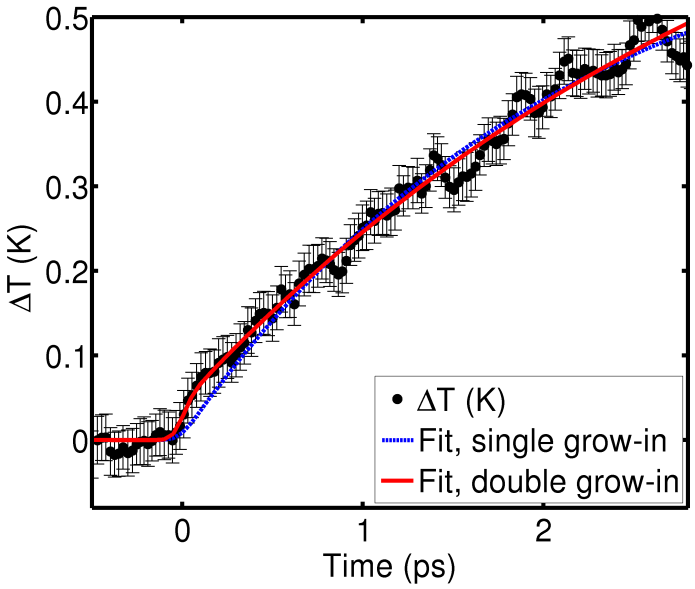

Figure S2. Time evolution of the temperature increase ΔT of the bulk-solvent modelled as a single (dashed blue) or a double (red) exponential grow-in (Eq. S5).

D. Error estimates

As utilized in our previous analysis of XDS data and described in detail in [4], the difference signal ΔS is known to be varying only slowly as a function of Q. We estimate the noise for each ΔS(Q,t) point from the high frequency fluctuations present in an interval around that point. Specifically, for every data point Q_p in the Q-range (with a total number

of $N = 500$ points), we fit a third-order polynomial to ΔS in a 50-point Q-interval around Q_p and estimate the noise σ at Q_p as the standard deviation of the residuals between data and polynomial fit in this interval.

The 'global' fitting procedure was implemented in Matlab®, utilizing constrained minimization of the standard χ^2 estimator:

$$\chi^2(\alpha, d_{\text{Co-Naxial}}, \Delta T) = \Big(\sum_{p=1}^{N} \frac{(\Delta S(Q_p)_{\text{model}} - \Delta S(Q_p)_{\text{meas.}})^2}{\sigma(Q_p)^2}\Big) \cdot \frac{1}{N - P - 1}. \qquad \text{(S6)}$$

where P is the number of free parameters.

The uncertainty estimates for $d_{\text{Co-Naxial}}$ and ΔT for each time point were calculated from the Hessian matrix returned by Matlab®. In the representation shown in Fig. 3 of the main article, $d_{\text{Co-Naxial}}$ was smoothed by a 4-point nearest neighbour filter (∼100 fs), reducing the estimated uncertainty on each point by a factor of two. The uncertainty on the initial excitation fraction A in Eq.7 was estimated as follows. A was allowed to range freely with the remaining fit parameters locked to their best-fit value, thus producing a 2D $\Delta S_{\text{model}}(Q,t)$ matrix for each value of the free parameter from which an average χ^2 could be computed by direct comparison with the measured data set through Eq. S6. These $\chi^2(A)$ curves were converted to a (relative) likelihood distribution $L(A)$ through $L = exp(-\chi^2/2)$ [5]. $L(A)$ was subsequently fitted with a Gaussian, and the error estimated as the σ of this Gaussian function [4].

II. ANISOTROPIC SIGNAL $\Delta S_{\text{ani.}}(Q,T)$ AND ESTIMATE OF σ_{IRF}

Fig. S3(a) shows the anisotropic contribution ($\Delta S_{\text{ani.}}$) to the total difference scattering signal, with the isotropic part (ΔS) shown in Fig. 2 and analysed in the main text. The two contributions were extracted from the 2D difference scattering patterns as detailed in [6]. As the excitation of the solute molecules have very little or no polarization dependence, the anisotropic component of the difference scattering signal arises from the almost instantaneous transient response of the water molecules to the electric field of the laser pulse (Kerr effect). The very fast nature of this response [7] allows us to use it to estimate the time resolution of the experiment. The response is found to be well described by the convolution of an exponential decay with a Gaussian IRF, and by fitting this model to the data we find σ_{IRF} = 0.05 ± 0.03 ps and t_0 = -0.01 ± 0.03 ps (see Fig. S3(b)). These values are assumed to

describe the IRF for the experiments presented in this work, and were kept fixed throughout the analysis described in the main text.

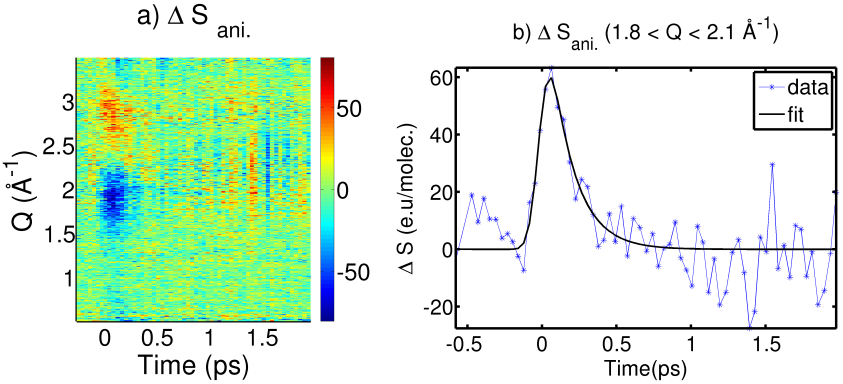

Figure S3. **a:** Anisotropic difference scattering signal $\Delta S_{ani.}(Q,t)$. **b:** Averaged value of $\Delta S_{ani.}$ in the interval 1.8 Å $< Q <$ 2.1 Å, where the scattering signature of the transient alignment of water molecules with the polarized laser pulse appears is most dominant. The expression in Eq. S3 is used for the fit.

III. SVD ANALYSIS

Fig. S4(a) shows the difference scattering signal $\Delta S_{Solv\text{-}subtr.}$ obtained after subtracting the (fitted, see above and main text for details) solvent contribution from ΔS (Q,t) (Fig.2). It is dominated by the negative feature at low-Q, signature of the expansion of the Co-N bonds. Fig. S4(b, c and d) show the main results of a Singular Value Decomposition (SVD) of this signal. As indicated by the relative magnitude of the singular values shown in Fig. S4(b), a single component dominates the signal. This component and its amplitude as a function of time are shown in Fig. S4(c) and Fig. S4(d), respectively.

With respect to the latter, the time evolution arises from both the structural dynamics and the kinetics of the bond-elongated state. Fig.S5 shows that, up to 0.5 ps, this time evolution is well-described by a grow-in exponential function followed by an oscillation, all broadened by the IRF:

$$V_1^{model}(t) = IRF(\sigma_{IRF}, t) \otimes [R(1 - e^{-\frac{t-t_0}{\tau_G}}) + O\cos(\frac{2\pi(t-t_0)}{T} + f)] \cdot H(t-t_0) \qquad (S7)$$

$$= \int_{t_0}^{+\infty} \frac{1}{\sigma_{IRF}\sqrt{2\pi}} e^{-\frac{(t-y)^2}{2\sigma_{IRF}^2}} [R(1 - e^{-\frac{y-t_0}{\tau_G}}) + O\cos(\frac{2\pi(y-t_0)}{T} + f)]dy$$

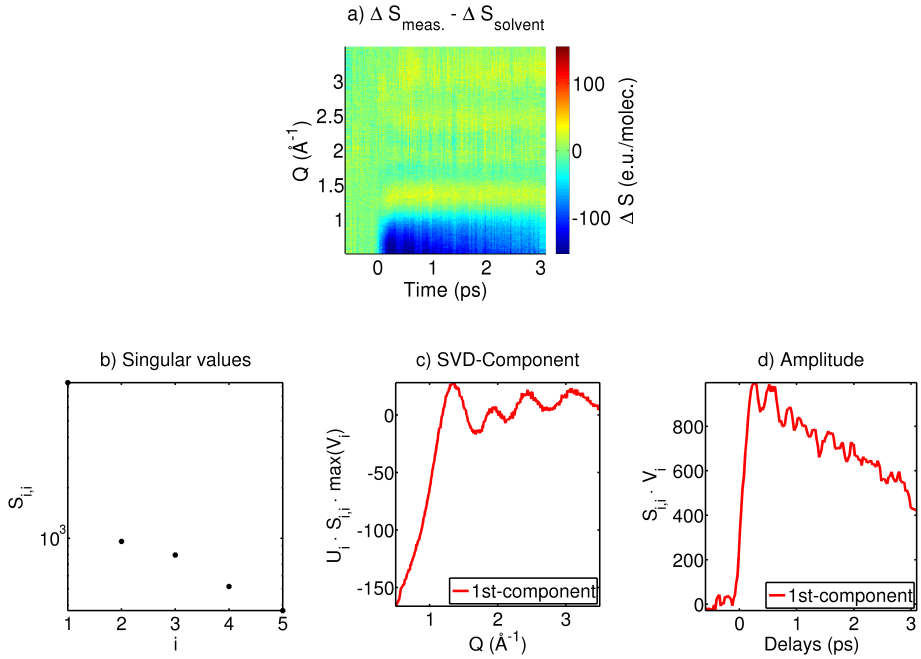

Figure S4. **a:** $\Delta S_{\text{Solv-subtr.}}$: difference scattering signal obtained by subtracting $\Delta S_{\text{solvent}}$ from the experimental data. **b-d:** Results of a SVD analysis of the data in **a**. $\Delta S_{\text{Solv-subtr.}} = U \cdot S \cdot V^{T}$. **b:** The singular values of the diagonal $S_{i,i}$. **c:** Q-profile of the first component ($U_1 \cdot S_{1,1} \cdot max(V_1)$). **d:** Temporal evolution of the first component ($S_{1,1} \cdot V_1$), smoothed by a 3-point nearest neighbour filter (∼75 fs).

where R and τ_G are the amplitude and the lifetime of the exponential, and O, T and f the amplitude, the period and the phase of the oscillation, respectively, and y is the integration variable. The values of both the fixed variables and the obtained parameters are reported in Tab. S3. The rise time of the structural signal is found to be 0.06 ps ± 0.01 ps and the phase shift of the oscillation, which has a period of ∼0.33 ps, is found to be 0.08 ps ± 0.02 ps. This is interpreted as an indication of the presence of one (or more) intermediate state(s) before the (electronic) population of the bond-elongated state, as further discussed in the main text.

σ_{IRF} (ps)	0.05 (fixed)
t_0 (ps)	-0.01 (fixed)
R (a.u.)	0.91 ± 0.03
τ_G (ps)	0.06 ± 0.01
O (a.u.)	0.09 ± 0.06
T (ps)	0.33 (fixed)
f (a.u.)	1.5 ± 0.4

Table S3. Fit results (95 % confidence bounds) after fitting the expression in Eq. S7 to the (normalized) amplitude of the first component after a SVD of $\Delta S_{\text{Solv-subtr.}}$ (Fig. S5).

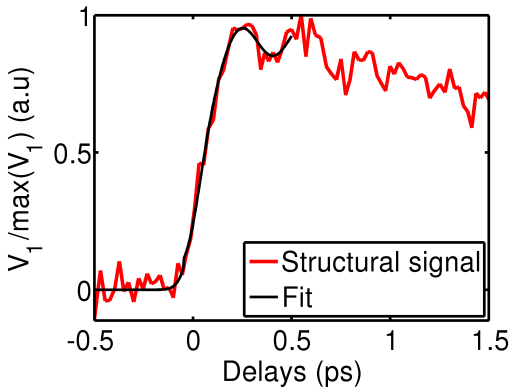

Figure S5. Temporal evolution of the (normalized) amplitude of the first component obtained from a SVD analysis of $\Delta S_{\text{Solv-subtr.}}$ (Fig. S4). We interpret this as the signal arising from primarily the change in the structure of the solute. The black line represents a fit to the data, utilizing a IRF-broadened exponential grow-in function with lifetime of 0.06 ps ± 0.01 ps followed by an oscillation of 0.33 ps period and with a 0.08 ps ± 0.02 ps phase shift.

IV. FOURIER TRANSFORM OF THE OSCILLATORY STRUCTURAL SIGNAL

Fig.S6(a) shows the temporal evolution of the structural contribution (red line) to the measured ΔS (see Fig. S4). This temporal evolution is described by a broadened exponential decay (black line). The residuals (blue line) between the data and the fit are here referred to as the oscillatory structural signal (OSS). Fig.S6(b) shows the Fourier Transform of the OSS for t > 0.3 ps: two main peaks are found at ∼0.23 ps and ∼0.34 ps. The inset of Fig.3

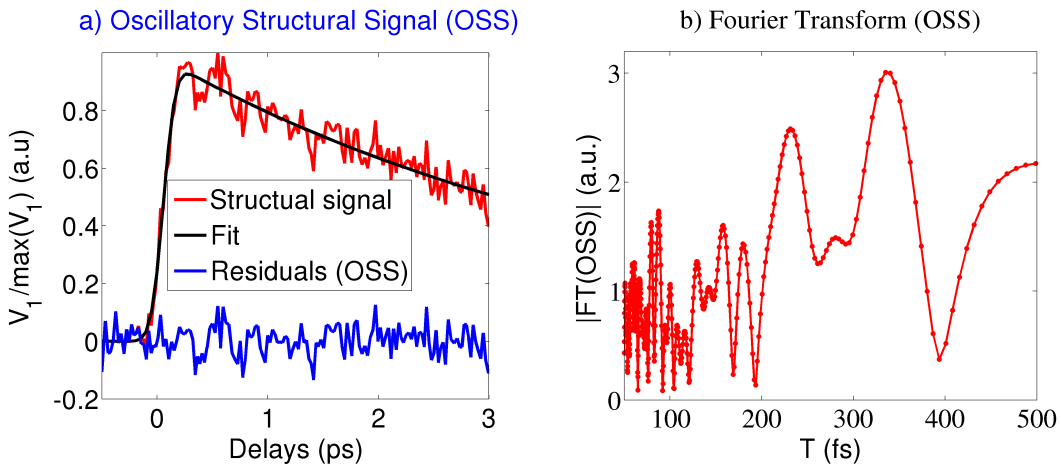

Figure S6. **a:** Amplitude of the first SVD component of $\Delta S_{Solv-subtr}$ (see Fig. S4) as a function of time (red). This represents the time evolution of the structural signal. An exponential decay broadened by a Gaussian function (black) is fitted to the data. Difference (blue) between the structural signal and the exponential fit. We refer to this as the oscillatory structural signal (OSS). **b:** Fourier Transform (FT) of the OSS for t > 0.3 ps, with the two main peaks at 220 fs and 340 fs.

in the main article shows the time dependent FT of the OSS obtained by sliding a 2 ps Hann window starting from a central value of 0.6 ps up to a central value of 2 ps.

V. LONG TIME RANGE MEASUREMENTS

Fig. S7(a) shows the isotropic difference scattering signals $\Delta S(Q, t)$ measured for time delays up to 20 ps. This dataset was binned in ∼300 fs bins, with 400 images in each bin. The following model was used to fit the data at each time delay:

$$\Delta S_{\text{model}}(Q, t) = \alpha(t)\Delta S_{\text{str.}}(Q) + \Delta T(t)\frac{\partial S(Q)}{\partial T}\bigg|_{\rho} \tag{S8}$$

with α and ΔT as free parameters and $\Delta S_{\text{struc.}}$ calculated from the structure of $[Co(terpy)_2]^{2+}$ 2 ps after the photoexcitation (as obtained from the analysis of the short time range dataset). This model can describe the data at all time delays, as indicated by the low residuals in Fig. S7(b). The time evolution of the kinetic parameters, α and ΔT are reported in Fig. S8. A single exponential decay is used to fit the excitation fraction α after 2 ps (i.e. after the excited-state structure has relaxed), and a lifetime of 6.8 ps ± 0.8 ps is found. The

temporal evolution of the temperature increase is well-described by a single exponential grow-in function (Eq. S5) and the obtained parameters are reported in Tab. S2.

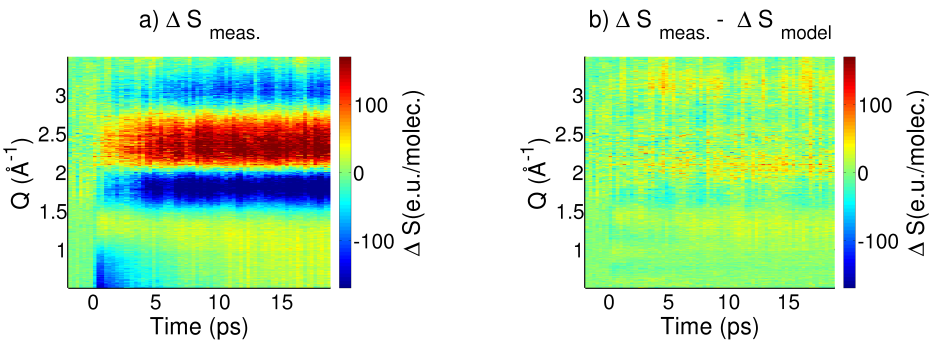

Figure S7. **a:** Measured difference scattering signal ($\Delta S_{meas.}(Q, t)$) of photoexcited $[Co(terpy)_2]^{2+}$ in aqueous solution (long time range dataset). **b:** Residuals obtained by subtracting the model (Eq. S8) from the experimental data.

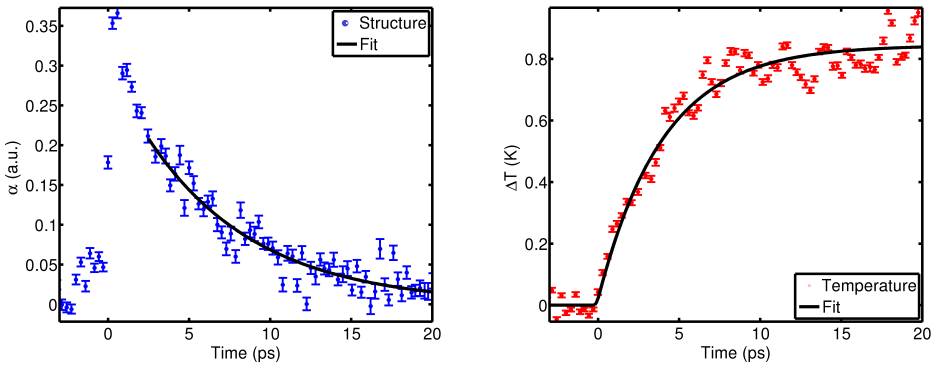

Figure S8. Kinetics obtained from the fit of the long time range dataset. **a:** Evolution of α, the magnitude of the structural component observed in the difference scattering signal (blue points). After 2 ps, it is well-described by an exponential decay with lifetime of 6.8 ps ± 0.8 ps (black line), interpreted as the lifetime of the bond-elongated HS excited state. **b:** Time evolution of the temperature increase ΔT of the solvent (red points). The temperature increase is well described by an exponential grow-in with a time constant of 4.0 ps ± 0.6 ps (Eq. S5).

VI. MD SIMULATIONS AND RDF ANALYSIS

The LS and HS structures of $[Co(terpy)_2]^{2+}$ were solvated in a cubic box (50 Å size) of water molecules using the TIP4P-Ew potential [8]. The bond lengths of the solute molecule were constrained and MD trajectories were calculated with OPLS2005 force field parameters [9] and a Nose-Hoover thermostat at 300 K [10]. The Radial Distribution Functions (RDFs) of the solute-solvent atom pairs were sampled in 0.1 Å radial bins and over 2000 individual simulation time steps over a total time interval of 2 ns. Fig. S9 shows the radial distribution functions (RDFs) g(r) of the oxygen (O) and hydrogen (H) atoms with respect to the Co atom, r being the distance from the Co, and the coordination number cn(r), the number of oxygens/hydrogens contained in a sphere of radius r, for both the LS and HS states of solvated $[Co(terpy)_2]^{2+}$. The first peak in the RDFs represents the first solvation shell. By inspection of $g_{CoO}(r)$ in Fig. S9(a), we note that the first peak slightly shifts (∼0.1 Å) towards smaller r values, decreases in amplitude and broadens upon the LS → HS spin transition on the Co centre. Considering the first minimum in the RDFs to be the limit of the first solvation shell, in the LS state it is found at 5.9 Å and, at this value, cn(r) is found to be ∼12 for both spin states. Similar considerations for $g_{CoH}(r)$ are shown in Fig. S9(b). This observation indicates that, upon the expansion of the Co-N bonds, the water molecules on average come closer (∼ 0.1 Å) to the Co-center but their total number in the first solvation shell remains constant. Finally, Fig. S9(c) shows that, relative to the H, the O come slightly closer to the positive Co centre in the HS spin with respect to the LS spin, representing a general rotation of the water molecules upon the spin transition.

VII. ENERGETICS

The laser pump energy absorbed by the solute molecules and the subsequent temperature increase of the solvent due to non-radiative relaxation of the solute can be estimated from experimental parameters, as detailed in [1]. Given a square X-ray spot size of $d_{X\text{-ray}} = 50$ μm, a path length (through the 45 ° tilted liquid sheet) of $l = 140$ μm and a sample concentration of $c = 20$mM, the number of molecules N_V in the probed volume can be calculated as:

$$N_V = c \cdot N_A \cdot d_{X\text{-ray}}^2 \cdot l = 4.2 \cdot 10^{12}$$

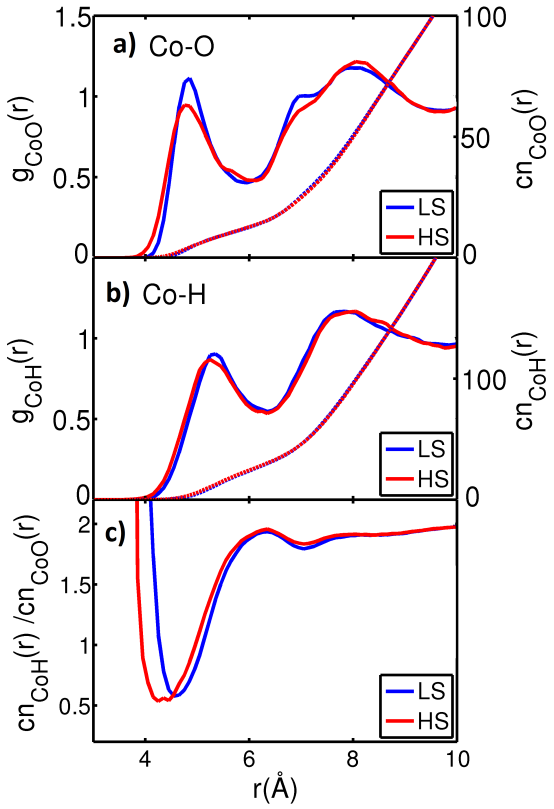

Figure S9. **a-b:** LS and HS RDFs g(r) of the water oxygen (**a**) and hydrogen (**b**) atoms with respect to the Co atom (solid line, left y-axis) and coordination number cn(r) (dashed lines, right y-axis) **c:** ratio of the Co-H to the Co-O coordination number in the LS and HS state, describing the orientation of the water molecules with respect to the Co center.

where N_A is Avogadro's number. Given an excitation fraction of 34 %, as found in our analysis, the number of excited molecule is then:

$$N_{\text{exc.}} = 0.34 \cdot N_V = 1.4 \cdot 10^{12}.$$

By assuming a linear regime such that each of these molecules absorbed one 530 nm photon (2.3 eV per photon), the energy per unit volume released to the solvent after non-radiative decay of the solute species would be:

$$E_{\text{dep.}} = \frac{N_{\text{exc.}} \cdot 2.3 \text{ eV}}{(50 \text{ cm})^2 \cdot l} = 1.5 \text{ J/cm}^3.$$

The specific heat capacity of water is $C_p = 4.18$ J$\cdot$ cm^{-3} $\cdot$ K^{-1} and the average temperature change in the volume probed by the X-ray would then be expected to be:

$$\Delta T = \frac{E_{\text{dep.}}}{C_p} = 0.38 \text{ K}$$

which is lower than the 0.84 K found from the analysis of the experimental dataset (Tab. S2). This we interpret as an indication that multi-photon excitation of the sample (solute and solvent) may be present and should be taken into account in the analysis. That such higher-order processes appear to be active is not surprising, as the excitation laser intensity is quite high. Given a laser pulse length of 70 fs and a laser pulse energy of 70 μJ focused on a spot of diameter of $d = 150$ μm (FHWM), the peak irradiance will be 3.5 TW/cm^2.

In order to further investigate the robustness of the results presented in the main article in the presence of multi-photon absorbtion, a second dataset with significantly lower laser power, 20 μJ (i.e. at a peak irradiance of 1 TW/cm^2), was subjected to the same analysis as that presented in the main text (Eq.5). For this dataset, we find an excitation fraction of 19 % and a 0.2 K temperature increase, as shown in Fig.S10(a). From the same energetics calculations as above, a temperature increase of 0.2 degrees indicates that the 20 μJ data set represents the response in the linear, one-photon excitation regime. Fig.S10(b) shows that the Co-N bond length dynamics results obtained from the analysis of the 20μJ dataset are essentially the same, but with more noise, than those obtained from the 70μJ dataset and presented in the main article.

As discussed in detail in our previously published LCLS studies, the presence of multi-photon excitation can result in very significant local heating of the solvent [11]. This may in turn lead to a breakdown in the assumption that the changes in scattering due to the temperature response of the aqueous solvent can be well described by a single, linearly scaled solvent differential. However, as also described in our recent work [11], the model describing the changes in solvent scattering can be readily extended to include a second-order term $\left.\frac{\partial^2 S(Q)}{\partial T^2}\right|_\rho$ which can be obtained from either MD modelling or from experiments [12]. Including this contribution in the full model, we found that it contributed at most 5 % of the measured difference signal and it was found to have no discernible impact on any of the results presented in this work. Including the second order solvent differential in the analysis of the 20 μJ indicated no contribution.

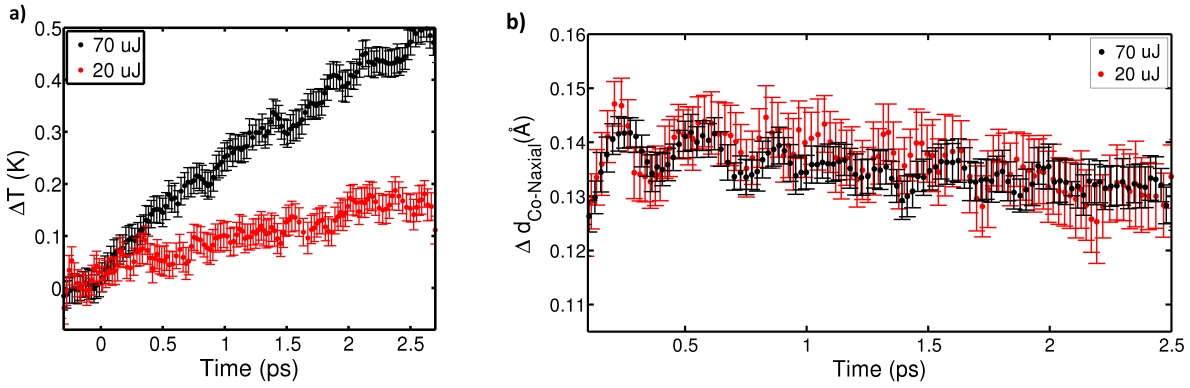

Figure S10. **a:** Time evolution of the temperature increase of the bulk-solvent after photoexcitation of the sample with a 20 μJ (red) or a 70 μJ (black) laser pulse. **b:** Time evolution of the changes in the Co-N bond length distance from the ground to the excited state after after photoexcitation with a 20 μJ (red) or a 70 μJ (black) laser pulse.

VIII. DFT CALCULATIONS

The DFT calculations were carried out with the ORCA program package [13, 14], utilizing the gradient-corrected BP86 exchange correlation functional [15, 16] in combination with the TZVP basis set. Solvent effects were approximated by the application of the conductor-like screening model (COSMO) using the relative permittivity of water ($\varepsilon = 80.4$). Vibrational frequencies were calculated as second derivatives of the electronic energy, and were all found to be positive, confirming that the optimized geometries at the BP86/TZVP level correspond to true minima of the corresponding potential energy surfaces (PES). Movie S1 shows the breathing mode of the HS state of $[Co(terpy)_2]^{2+}$, using the vectors and the frequency (92 cm^{-1}) obtained from DFT calculation. From the same calculation, Movie S2 shows the 'pincer-like' mode found at 146 cm^{-1}.

IX. EXPERIMENTAL SETUP AND DATA REDUCTION

The 20 mM aqueous solution of $Co(terpy)_2Cl_2$ was prepared according to the procedure given in [17]. Fig.S11 shows the absorption spectrum of $[Co(terpy)_2]^{2+}Cl_2$ in water. For the experiment, the solution was pumped through a sapphire nozzle producing a 100 µm flat liquid sheet flowing in the vertical direction and inclined at 45° to the (nearly) collinear

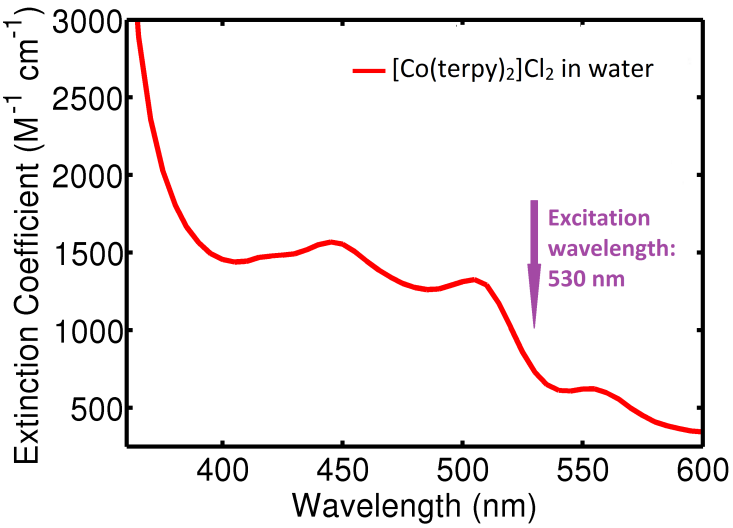

Figure S11. UV-Vis absorption spectrum of $[Co(terpy)_2]^{2+}$ in water.

co-propagating laser and X-ray beams. The flow rate (ca. 1 mm/ms) was sufficient to fully replace the sample between successive X-ray pulses at the 120 Hz repetition rate of the LCLS facility. The laser system produced 70 μJ pulses at 530 nm with 70 fs pulse width (FWHM) and 7.5 nm bandwidth (FWHM). It was focused onto a 150 μm diameter spot (via a CaF_2 lens with 750 mm focal length). The 8.3 keV X-ray probe pulses (with $\sim 10^{12}$ photons/pulse on average) were focused to a (50 μm)^2-size square spot and overlapped with the pump laser at the sample position. The laser excited the sample synchronously for every probing X-ray pulse, except for every 5th pulse, where the laser beam was dropped before the sample position, so that the static structure of the sample with only ground state species present could be repeatedly measured during the sequence of pump-probe XDS measurements. The acquired 2D scattering patterns were corrected for artefacts due to X-ray pulse energy and intensity shot-to-shot jitter following the procedure described by van Driel et al. [18]. The patterns were then corrected for X-ray polarization, solid-angle and absorption through the liquid sheet. The radially integrated scattering signal from each pattern was scaled to the total 1D scattering signal calculated in electron units for a liquid unit cell, which, in the present experiment, consists of one solute molecule, 2777 water molecules and two Cl atoms. The full Q range [0.5 - 3.5] $Å^{-1}$ was used as scaling interval and the so-obtained scaling factor was then used to scale each 2D pattern. Individual 2D difference scattering images were obtained by subtracting the laser-off from the laser-on scattering patterns. In

order to extract the temporal behaviour during a time-delay scan between laser and X-ray pulses, the time-corrected images (using the XPP timing tool [19]) were sorted into ∼23 fs wide bins with 600 difference scattering patterns being averaged in each. 1D isotropic and anisotropic difference scattering signals were extracted from each of these averaged 2D difference patterns. For the set of measurements described here, the relative intensity of the difference signal was on the order of 0.1 % of the total scattering signal.

[1] K. S. Kjaer, T. B. van Driel, J. Kehres, K. Haldrup, D. Khakhulin, K. Bechgaard, M. Cammarata, M. Wulff, T. J. Sørensen, and M. M. Nielsen, Physical Chemistry Chemical Physics **15**, 15003 (2013).

[2] T. J. Sørensen and K. S. Kjær, (2013), https://sites.google.com/site/trwaxs/.

[3] J. Als-Nielsen and D. McMorrow, "X-rays and their interaction with matter," in *Elements of Modern X-ray Physics* (John Wiley and Sons, Inc., 2011) pp. 1–28.

[4] K. Haldrup, M. Christensen, and M. Meedom Nielsen, Acta Crystallographica Section A **66**, 261 (2010).

[5] S. Jun, J. H. Lee, J. Kim, J. Kim, K. H. Kim, Q. Kong, T. K. Kim, M. Lo Russo, M. Wulff, and H. Ihee, Physical Chemistry Chemical Physics **12**, 11536 (2010).

[6] U. Lorenz, K. B. Møller, and N. E. Henriksen, New Journal of Physics **12**, 113022 (2010).

[7] S. Palese, L. Schilling, R. J. D. Miller, P. R. Staver, and W. T. Lotshaw, The Journal of Physical Chemistry **98**, 6308 (1994).

[8] H. W. Horn, W. C. Swope, J. W. Pitera, J. D. Madura, T. J. Dick, G. L. Hura, and T. Head-Gordon, The Journal of Chemical Physics **120**, 9665 (2004).

[9] W. L. Jorgensen et al., Journal of the American Chemical Society **118**, 11225–11236 (1996).

[10] G. J. Martyna, M. L. Klein, and M. Tuckerman, The Journal of Chemical Physics **97**, 2635 (1992).

[11] K. Haldrup, W. Gawelda, R. Abela, R. Alonso-Mori, U. Bergmann, A. Bordage, M. Cammarata, S. Canton, A. Dohn, T. van Driel, D. Fritz, A. Galler, P. Glatzel, T. Harlang, K. Kjær, H. Lemke, K. Moller, Z. Németh, M. Pápai, N. Sas, J. Uhlig, D. Zhu, G. Vankó, V. Sundstrom, M. Nielsen, and C. Bressler, The Journal of Physical Chemistry B **120**, 1158 (2016).

[12] J. Neuefeind, C. J. Benmore, J. K. R. Weber, and D. Paschek, Molecular Physics **109**, 279 (2011).

[13] ORCA version 3.0.3, F. Neese, Max-Planck-Institut für Chemische Energiekonversion, https://orcaforum.cec.mpg.de/.

[14] F. Neese, WIREs Computational Molecular Science **2**, 73 (2012).

[15] A. D. Becke, Physical Review A **38**, 3098 (1988).

[16] J. P. Perdew, Physical Review B **33**, 8822 (1986).

[17] R. A. Binstead and J. K. Beattie, Inorganic Chemistry **25**, 1481 (1986).

[18] T. B. van Driel, K. S. Kjaer, E. Biasin, K. Haldrup, H. T. Lemke, and M. M. Nielsen, Faraday Discussions **177**, 443 (2015).

[19] M. P. Minitti, J. S. Robinson, R. N. Coffee, S. Edstrom, S. Gilevich, J. M. Glownia, E. Granados, P. Hering, M. C. Hoffmann, A. Miahnahri, and et al., Journal of Synchrotron Radiation **22**, 526 (2015).